J. Fluid Mech. (2000), *vol.* 417, *pp.* 211–236. Printed in the United Kingdom

Flow past a sphere moving vertically in a stratified diffusive fluid

By C. R. TORRES[1], H. HANAZAKI[2]†, J. OCHOA[3], J. CASTILLO[4] AND M. VAN WOERT[5]

[1]Instituto de Investigaciones Oceanológicas, Universidad Autónoma de Baja California, A. P. 453, 22800 Ensenada, Baja California, México

[2]Institute of Fluid Science, Tohoku University, 2-1-1 Katahira, Aoba-ku, Sendai 980-8577, Japan

[3]Centro de Investigación Científica y de Educación Superior de Ensenada, Km 107 Carr. Tijuana-Ensenada, Ensenada, B. C., México

[4]Department of Mathematics, San Diego State University, San Diego, CA 92812-0314, USA

[5]NOAA/NESDIS/Office of Research and Applications. World Weather Building Rm-711, 4700 Silver Hill Road Stop, Washington DC 20233-9910, USA

(Received 7 December 1999 and in revised form 23 March 2000)

Numerical studies are described of the flows generated by a sphere moving vertically in a uniformly stratified fluid. It is found that the axisymmetric standing vortex usually found in homogeneous fluids at moderate Reynolds numbers ($25 \leqslant Re \leqslant 200$) is completely collapsed by stable stratification, generating a strong vertical jet. This is consistent with our experimental visualizations. For $Re = 200$ the complete collapse of the vortex occurs at Froude number $F \simeq 19$, and the critical Froude number decreases slowly as Re increases. The Froude number and the Reynolds number are here defined by $F = W/Na$ and $Re = 2Wa/\nu$, with W being the descent velocity of the sphere, N the Brunt–Väisälä frequency, a the radius of the sphere and ν the kinematic viscosity coefficient. The inviscid processes, including the generation of the vertical jet, have been investigated by Eames & Hunt (1997) in the context of weak stratification without buoyancy effects. They showed the existence of a singularity of vorticity and density gradient on the rear axis of the flow and also the impossibility of realizing a steady state. When there is no density diffusion, all the isopycnal surfaces which existed initially in front of the sphere accumulate very near the front surface because of density conservation and the fluid in those thin layers generates a rear jet when returning to its original position. In the present study, however, the fluid has diffusivity and the buoyancy effects also exist. The density diffusion prevents the extreme piling up of the isopycnal surfaces and allows the existence of a steady solution, preventing the generation of a singularity or a jet. On the other hand, the buoyancy effect works to increase the vertical velocity to the rear of the sphere by converting the potential energy to vertical kinetic energy, leading to the formation of a strong jet. We found that the collapse of the vortex and the generation of the jet occurs at much weaker stratifications than those necessary for the generation of strong lee waves, showing that jet formation is independent of the internal waves. At low Froude numbers ($F \leqslant 2$) the lee wave patterns showed good agreement with the linear wave theory and the previous experiments by Mowbray & Rarity (1967). At very low Froude numbers ($F \leqslant 1$) the drag on a sphere increases rapidly, partly due to the lee

† Also Department of Mechanical Engineering, University of Tokyo, 7-3-1 Hongo, Bunkyo-ku, Tokyo 113-8656, Japan.

wave drag but mainly due to the large velocity of the jet. The jet causes a reduction of the pressure on the rear surface of the sphere, which leads to the increase of pressure drag. High velocity is induced also just outside the boundary layer of the sphere so that the frictional drag increases even more significantly than the pressure drag.

1. Introduction

Most of the previous studies on stratified flows have been devoted to horizontal flows since many typical flows relevant to geophysical phenomena, such as mountain gravity waves, are horizontal. Indeed, we often observe extraordinary phenomena due to the buoyancy effects in stratified horizontal flows, including the collapse of the standing vortex and the subsequent generation of horizontal eddies downstream of an obstacle at strong stratification (Hunt & Snyder 1980). In particular, horizontal flows of stratified fluids past a sphere have been studied experimentally by Lofquist & Purtell (1984), Lin *et al.* (1992) and Chomaz, Bonneton & Hopfinger (1993) among others, and numerically by Hanazaki (1988).

On the other hand, vertical flows are also important, particularly in their application to the aerosol diffusion in the atmosphere and upper ocean biogeochemistry. For example, the settling of conglomerates of organic materials which sink rapidly in the ocean controls the rate of nutrient regeneration and links the pelagic and benthic food webs (Billet *et al.* 1983; Graf 1989).

The flow around a vertically moving obstacle in stratified fluid, however, has not been studied extensively. The lee wave far behind a sphere has been studied experimentally by Mowbray & Rarity (1967) at low Froude numbers ($0.4 \leqslant F \leqslant 2$) with a moderate Reynolds number ($Re \leqslant 200$), but little attention has been paid to the flow near the obstacle. Mowbray & Rarity mention that 'no systematic study was made of the behaviour of fluid in the boundary layer or in the wake, other than ensure that periodic vortices were not generated'. Indeed, although a thin vertical streak can be identified in the shadowgraphs by Mowbray & Rarity (their plate 1 or figure 106 of Lighthill 1978), no explanations have been given of that phenomenon. Our results will clarify that this thin streak appears along with the collapse of the standing vortex usually found in homogeneous fluids. It takes the form of a long narrow filament and the velocity distributions obtained in our numerical study show that it is actually a strong jet along the vertical axis.

The change of the downstream wake patterns with increasing stratification obtained by earlier shadowgraph experiments (Ochoa & Van Woert 1977) is shown in figure 1. The figure shows that at weak stratifications with a moderate Reynolds number ($F = 25.81$, $Re = 800$) a standing vortex exists just as in homogeneous fluids (figure 1*a*). Increasing stratification ($F = 12.64$, $Re = 800$) causes complete vortex collapse and the generation of a long narrow filament or jet (figure 1*b*). At stronger stratification ($F = 4.21$, $Re = 762$), the filament/jet becomes narrower (figure 1*c*). The Froude number and the Reynolds number are here defined by $F = W/Na$ and $Re = 2Wa/\nu$, with W being the descent velocity of the sphere, N the Brunt–Väisälä frequency, a the radius of the sphere and ν the kinematic viscosity coefficient.

It is of interest to note that near axisymmetry of the flow is retained even at $Re \simeq 800$, well above the critical Reynolds number ($\simeq 500$) for the onset of vortex shedding in homogeneous fluids. The parameter region $(Re, 1/F)$ which classifies the

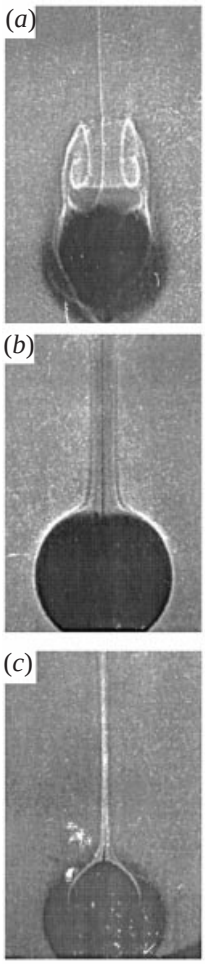

FIGURE 1. Shadowgraphs of the flow around a sphere moving vertically in a stratified fluid. (*a*) $(F, Re) = (25.81, 800)$; (*b*) $(12.64, 800)$; (*c*) $(4.21, 762)$.

downstream wake patterns is shown in the Appendix (figure 16) along with a brief explanation of the experimental methods used in Ochoa & Van Woert (1977).

In this numerical study we investigate the mechanisms of vortex collapse and the subsequent generation of the rear filament/jet as the stratification increases. The collapse and the jet formation occur well before the generation of the strong lee waves, showing that the jet formation is almost independent of the internal wave generation. At low Froude numbers we show the generation of internal wave patterns in agreement with the linear theory and the experiments by Mowbray & Rarity (1967). We show however that a stronger jet is generated at lower Froude numbers due to buoyancy effects.

Figure 2 shows the parameter region $(Re, 1/F)$ investigated in this study. The experiments by Ochoa & Van Woert (1977) lie inside the diamond-shaped region covering the area $200 < Re < 4000$ and $0.028 < 1/F < 0.265$ $(3.77 < F < 35.35)$. The solid line within the diamond region separates the upper region where the downstream filaments were observed from the lower region where vortical wakes as in homogeneous fluids were observed (cf. figure 16). The shaded region denotes the

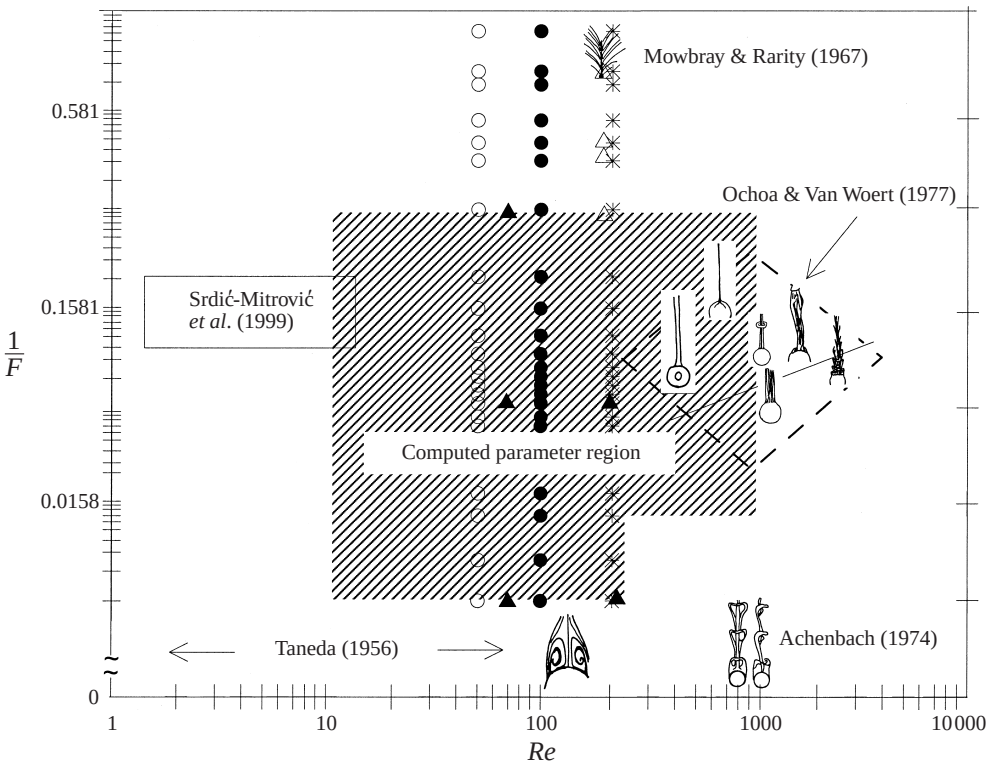

FIGURE 2. Parameter range of this numerical study and previous experimental studies. The shaded area represents the parameter region investigated in this numerical study. The diamond-shaped region denotes the region investigated experimentally by Ochoa & Van Woert (1977). A solid line is drawn in that region, above which the filament wakes exist and below which vortical wakes similar to those observed in homogeneous flows exist. The small triangles denote the representative cases discussed in §4. The other symbols represent the data used in figures 8 and 11.

computed parameter region in this study and the triangles specify the cases used for the discussion in §4, including the comparison with experiments by Mowbray & Rarity (1967).

Recently, during the revision of this paper, we came across the experiments by Srdić-Mitrović, Mohamed & Fernando (1999) which investigated the flow around small spherical particles moving vertically across a density interface. In their experiments, the top and bottom layers are homogeneous fluids with different densities, with an interfacial layer of approximately uniform stratification between them. A spherical particle in the diameter range of 0.25–1.80 mm was released in the upper homogeneous layer and it descended through the stratified interfacial layer of 2–4 cm to the bottom homogeneous layer.

In the parameter range of $1.5 \leqslant Re \leqslant 15$ and $3 < F < 10$ $(0.1 < 1/F < 0.33)$ (see figure 2), they found an elongated tail or a caudal fluid column dragged from the upper homogeneous layer. The dragging of the fluid from the upper homogeneous layer is known from two-layer fluid experiments in chemical engineering, but they investigated the effect of continuous stratification on the caudal fluid column. Thus, their experiments have much more similarity to the present study. Their flow was unsteady, however. The caudal fluid column is generated once and it is ruptured with time. In their study the time-development of the descending velocity was measured

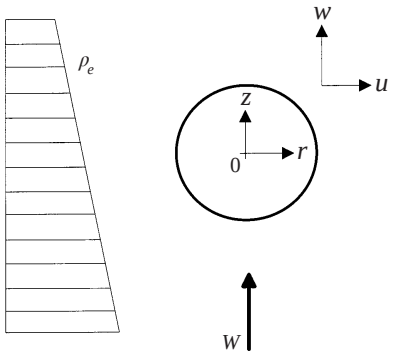

FIGURE 3. A schematic description of the vertical flow of stratified fluid past a sphere.

to estimate the drag on a particle. They found that the drag coefficient was an order of magnitude larger than its homogeneous counterpart and most of the contribution comes from the static effect of buoyancy force due to the bulk of caudal fluid dragged from the upper layer. Therefore, the internal-wave contribution to the stratification drag was estimated to be small.

To our knowledge, ours is the first study on the effect of continuous and uniform stratification throughout the fluid. We found, however, some similarities to the results of Srdić-Mitrović *et al.* (1999) which had discontinuities in stratification. For example, the drag increases much more than the prediction of the linear wave drag (Warren 1960), showing that the rear caudal fluid column in their study or the filament/jet in the present study is essential for the increase of the drag. We investigate the structure of the rear jet and the pressure distributions around the sphere to clarify the mechanisms of drag increase in the steady flow of the wholly continuously stratified fluid.

2. Basic equations

We consider a sphere moving downward at a constant speed in a uniformly stratified fluid. This is equivalent to an upward flow of a uniformly stratified fluid past a sphere (see figure 3). We assume that the density is diffusive. The diffusion of density is essential, particularly when we consider an obstacle which moves 'vertically' in a stratified fluid. In that case, if there is no diffusion ($\kappa = 0$ in equation (2) below), density is conserved along the flow direction of the fluid and all the isopycnals which initially existed in front of the obstacle accumulate very close to its front surface. Then, the vertical density gradient just ahead of the sphere increases without limit. This not only causes technical problems in computation but also prevents the flow from reaching steady state. We consider therefore a stratified fluid with density diffusion. This constitutes a realistic problem directly corresponding to the laboratory experiments and at the same time avoids the above difficulty inherent in non-diffusive fluid.

The governing equations for the flow of a stratified diffusive fluid with viscosity are

$$\tilde{\rho}\frac{\mathrm{D}\tilde{\boldsymbol{u}}}{\mathrm{D}\tilde{t}} = -\tilde{\nabla}\tilde{p} - \tilde{\rho}g\hat{\boldsymbol{z}} + \mu\tilde{\nabla}^2\tilde{\boldsymbol{u}}, \tag{1}$$

$$\frac{\mathrm{D}\tilde{\rho}}{\mathrm{D}\tilde{t}} = \kappa\tilde{\nabla}^2\tilde{\rho}, \tag{2}$$

and

$$\tilde{\nabla} \cdot \tilde{\boldsymbol{u}} = 0, \tag{3}$$

where $\tilde{t}$ is the time, $\tilde{\boldsymbol{u}} = (\tilde{u}, \tilde{v}, \tilde{w})$ is the velocity, $\tilde{p}$ is the pressure, $\tilde{\rho}$ is the density, g is the acceleration due to gravity, $\hat{\boldsymbol{z}}$ is the unit vector in the vertical direction, μ is the viscosity coefficient and κ is the diffusivity coefficient. Equation (3) represents mass conservation under the assumption that the term $\tilde{\rho}^{-1}\,\mathrm{D}\tilde{\rho}/\mathrm{D}\tilde{t}$ is negligibly small. This approximation is justified provided the density variation in the vertical direction is small.

When the fluid moves upward past the sphere at a constant velocity W, the basic fluid density ρ_e and the hydrostatic pressure p_e, which change continuously with time at a fixed height $\tilde{z}$, are given by

$$\rho_e(\tilde{z}, \tilde{t}) = \rho_o + \frac{\partial \rho_e}{\partial \tilde{z}}(\tilde{z} - W\tilde{t}), \tag{4}$$

and

$$p_e(\tilde{z}, \tilde{t}) = -\int^{\tilde{z}} \rho_e(\tilde{z}, \tilde{t}) g \, \mathrm{d}\tilde{z}, \tag{5}$$

where $\partial \rho_e/\partial \tilde{z}$ is the vertical gradient of the undisturbed density field which is assumed to be a constant here, and $\rho_o = \rho_e(\tilde{z} = 0, \tilde{t} = 0)$ is a reference density.

We decompose the density and the pressure into the basic states and their perturbations $\widehat{\rho}$ and $\widehat{p}$ respectively. Then the total density and pressure can be written as

$$\tilde{\rho} = \rho_e(\tilde{z}, \tilde{t}) + \widehat{\rho}, \tag{6}$$

and

$$\tilde{p} = p_e(\tilde{z}, \tilde{t}) + \widehat{p}. \tag{7}$$

Inserting (6) and (7) into (1), subtracting the basic state and using the Boussinesq approximation, it follows that

$$\frac{\mathrm{D}\tilde{\boldsymbol{u}}}{\mathrm{D}\tilde{t}} = -\frac{1}{\rho_o}\nabla\widehat{p} - \frac{\widehat{\rho}}{\rho_o} g\hat{\boldsymbol{z}} + \nu\tilde{\nabla}^2\tilde{\boldsymbol{u}}, \tag{8}$$

where $\nu = \mu/\rho_o$ is the kinematic viscosity. Similarly, substitution of (6) into (2) gives

$$\frac{\mathrm{D}\widehat{\rho}}{\mathrm{D}\tilde{t}} = -\frac{\partial \rho_e}{\partial \tilde{z}}(\tilde{w} - W) + \kappa\tilde{\nabla}^2\widehat{\rho}. \tag{9}$$

To obtain the non-dimensional version of (8) and (9), we scale distance by the radius of the sphere a, velocities by the sphere velocity W, pressure perturbation by $\rho_o W^2$, and density perturbation by $-a\partial\rho_e/\partial\tilde{z}$. Dropping the tildes and the hats that denote non-dimensional variables, the resulting set of equations becomes

$$\frac{\mathrm{D}\boldsymbol{u}}{\mathrm{D}t} = -\nabla p - \frac{1}{F^2}\rho\hat{\boldsymbol{z}} + \frac{2}{Re}\nabla^2\boldsymbol{u}, \tag{10}$$

and

$$\frac{\mathrm{D}\rho}{\mathrm{D}t} = w - 1 + \frac{2}{Pe}\nabla^2\rho. \tag{11}$$

The Péclet number Pe is defined by $Pe = Re\,Sc$ using the Schmidt number $Sc\,(= \nu/\kappa)$, and N is the Brunt–Väisälä frequency defined by

$$N^2 = -\frac{g}{\rho_o}\frac{\partial \rho_e}{\partial \tilde{z}}.$$

The Schmidt number Sc used in the definition of the Péclet number Pe must be replaced by the Prandtl number Pr if the stratification is due to a temperature difference.

Since the system of equations (3), (10) and (11) does not contain a term which explicitly represents the time development of the pressure, we have to formulate a diagnostic Poisson equation for the pressure which will become a substitute for the incompressibility condition given by (3). This is accomplished by taking the divergence of (10) (see also § 3). Hence, the governing equations to be solved are (10), (11) and

$$\nabla^2 p = -\frac{1}{F^2}\nabla\cdot(\rho\hat{\boldsymbol{z}}) - \nabla\cdot[(\boldsymbol{u}\cdot\nabla)\boldsymbol{u}] + \frac{2}{Re}\nabla^2 D - \frac{\partial D}{\partial t}, \tag{12}$$

where $D = \nabla\cdot\boldsymbol{u}$. We need a special treatment for D in the actual numerical discretization as will be shown later in the discussion of equation (24). The flow geometry allows axisymmetric solutions to be sought at relatively low Reynolds numbers (figure 3). This axisymmetry assumption is justified by experiments for $Re < 200$ in unstratified fluids (Taneda 1956) and sometimes even for $Re > 200$ in stably stratified fluids (Ochoa & Van Woert 1977). For example, our experiments (figure 1) show that the axisymmetric flow is retained for Reynolds numbers well above 200, which is the upper limit for axisymmetry in homogeneous flow. The vortex shedding and the transition to turbulence can be inhibited by stratification.

We use cylindrical coordinates with r the radial coordinate in the horizontal direction and z the vertical coordinate along the symmetry axis of the flow. The velocity vector is given by $\boldsymbol{u} = (u, w)$, where u is the r-component and w is the z-component (figure 3). Since the flow is axisymmetric and the velocity satisfies the divergence-free condition (3), we can define the Stokes stream function ψ by

$$u = -\frac{1}{r}\frac{\partial\psi}{\partial z}, \quad w = \frac{1}{r}\frac{\partial\psi}{\partial r}.$$

The sphere surface is assumed to be insulating so that there is no density flux across it. Then, the boundary conditions become as follows.

On the sphere surface ($z^2 + r^2 = 1$), the velocity satisfies the no-slip condition

$$u = w = 0. \tag{13}$$

The boundary condition of no density flux can be written first in dimensional form as

$$\tilde{\nabla}\tilde{\rho}\cdot\hat{\boldsymbol{n}} = 0, \tag{14}$$

where $\hat{\boldsymbol{n}}$ is the unit normal to the sphere surface. Then, the substitution of (6) into (14) gives

$$\tilde{z}\left(\frac{\partial\rho_e}{\partial\tilde{z}} + \frac{\partial\hat{\rho}}{\partial\tilde{z}}\right) + \tilde{r}\frac{\partial\hat{\rho}}{\partial\tilde{r}} = 0, \tag{15}$$

which in non-dimensional form becomes

$$z\frac{\partial\rho}{\partial z} + r\frac{\partial\rho}{\partial r} = -z. \tag{16}$$

The surface boundary condition for the pressure obtained from (10) is

$$\nabla p = -\frac{1}{F^2}\rho\hat{\boldsymbol{z}} + \frac{2}{Re}\nabla^2\boldsymbol{u}. \tag{17}$$

Far from the sphere, due to viscosity, diffusivity and geometrical spreading effects, all the physical quantities asymptote to their unperturbed values. Then, on the outer

boundary of the computed domain the pressure is extrapolated assuming zero normal derivative

$$\frac{\partial p}{\partial n} = 0, \tag{18}$$

and the density perturbation is assumed to vanish, i.e.

$$\rho = 0. \tag{19}$$

On the downstream (upper) outer boundary the velocities are extrapolated using

$$\frac{\partial u}{\partial z} = \frac{\partial w}{\partial z} = 0, \tag{20}$$

while on the upstream (lower) boundary they are fixed to be

$$u = 0, \quad w = 1. \tag{21}$$

3. The numerical method

The computations were performed on HP9000-735 and Origin2000 Silicon Graphics computers using the MAC (marker and cell) method which was originally developed by Harlow & Welch (1965) and was extended to incompressible stratified flows by Hanazaki (1988), in which the non-divergence of velocity can be similarly applied. The method has been used in other numerical studies of stratified flows (e.g. Hanazaki 1989, 1994) and also has been used to simulate the stratified flows with density diffusion (Torres 1997; Torres *et al.* 1999).

We use the explicit Euler method for the time development. Then, the equations (10), (11) and (12) become

$$\frac{\boldsymbol{u}^{n+1} - \boldsymbol{u}^n}{\Delta t} + (\boldsymbol{u}^n \cdot \nabla)\boldsymbol{u}^n = -\nabla p^n - \frac{1}{F^2}\rho^n \hat{\boldsymbol{z}} + \frac{2}{Re}\nabla^2 \boldsymbol{u}^n, \tag{22}$$

$$\frac{\rho^{n+1} - \rho^n}{\Delta t} + (\boldsymbol{u}^n \cdot \nabla)\rho^n = w^n - 1 + \frac{2}{Pe}\nabla^2 \rho^n, \tag{23}$$

and

$$\nabla^2 p^n = -\frac{1}{F^2}\nabla \cdot (\rho^n \hat{\boldsymbol{z}}) - \nabla \cdot [(\boldsymbol{u}^n \cdot \nabla)\boldsymbol{u}^n] + \frac{2}{Re}\nabla^2 D^n - \frac{D^{n+1} - D^n}{\Delta t}, \tag{24}$$

where the superscript n denotes the integration time $t = n\Delta t$. In the MAC method, D^{n+1} in (24) is set equal to zero while D^n is retained to prevent the accumulation of numerical round-off errors and to simultaneously implement the divergence-free condition given by equation (3).

Given the values of $\boldsymbol{u}$ and ρ at time step n ($n = 0$ corresponds to the initial condition), the Poisson equation (24) for the pressure p^n can be solved using the SOR (successive over-relaxation) method. Then substituting the obtained p^n into (22) and (23), the values of $\boldsymbol{u}$ and ρ at the next time step $t = (n+1)\Delta t$ are obtained. This cycle is repeated in the succeeding time steps.

The equations (22), (23) and (24) constitute a time-developing problem, but in this study we are interested in the steady solutions. Therefore, the process is repeated until the convergence criterion $|f^{n+1} - f^n|_{max}/(f^n_{max} - f^n_{min}) \leqslant 10^{-4}$ is satisfied, where f represents any one of u, w, p or ρ.

3.1. *Transformation to curvilinear coordinates*

To generate a numerical grid which resolves both the velocity and density boundary layers and at the same time to simplify the implementation of boundary conditions, a transformation of coordinates from the physical plane (z, r) to the computational plane (ξ, η) is performed. In general, the transformation is given by

$$z = z(\xi, \eta), \quad r = r(\xi, \eta), \tag{25}$$

and the equations (22), (23) and (24) become

$$\frac{w^{n+1} - w^n}{\Delta t} + \frac{u^n r_\eta - w^n z_\eta}{J} w_\xi^n + \frac{w^n z_\xi - u^n r_\xi}{J} w_\eta^n = -\frac{r_\eta p_\xi^n - r_\xi p_\eta^n}{J} - \frac{1}{F^2}\rho^n + \frac{2}{Re}\nabla^2 w^n, \tag{26}$$

$$\frac{u^{n+1} - u^n}{\Delta t} + \frac{u^n r_\eta - w^n z_\eta}{J} u_\xi^n + \frac{w^n z_\xi - u^n r_\xi}{J} u_\eta^n = -\frac{z_\xi p_\eta^n - z_\eta p_\xi^n}{J} + \frac{2}{Re}\left(\nabla^2 u^n - \frac{u^n}{r^2}\right), \tag{27}$$

$$\frac{\rho^{n+1} - \rho^n}{\Delta t} + \frac{u^n r_\eta - w^n z_\eta}{J} \rho_\xi^n + \frac{w^n z_\xi - u^n r_\xi}{J} \rho_\eta^n = w^n - 1 + \frac{2}{Pe}\nabla^2 \rho^n, \tag{28}$$

and

$$\nabla^2 p^n = -\frac{(r_\eta u_\xi^n - r_\xi u_\eta^n)^2 + 2(z_\xi u_\eta^n - z_\eta u_\xi^n)(r_\eta w_\xi^n - r_\xi w_\eta^n) + (z_\xi w_\eta^n - z_\eta w_\xi^n)^2}{J^2} + \frac{(r_\eta u_\xi^n - r_\xi u_\eta^n + z_\xi w_\eta^n - z_\eta w_\xi^n)}{J\Delta t} - \frac{1}{JF^2}(z_\xi \rho_\eta^n - z_\eta \rho_\xi^n), \tag{29}$$

where the subscripts ξ and η denote partial differentiation and the Laplacian operator ∇^2 is defined in the computational plane by

$$\nabla^2 A = \frac{(\alpha A_{\xi\xi} - 2\beta A_{\xi\eta} + \gamma A_{\eta\eta})}{J^2} + \frac{(\alpha z_{\xi\xi} - 2\beta z_{\xi\eta} + \gamma z_{\eta\eta})(r_\xi A_\eta - r_\eta A_\xi) + (\alpha r_{\xi\xi} - 2\beta r_{\xi\eta} + \gamma r_{\eta\eta})(z_\eta A_\xi - z_\xi A_\eta)}{J^3}. \tag{30}$$

The Jacobian of the transformation, J, and the transform coefficients α, β and γ are given by

$$J = z_\xi r_\eta - z_\eta r_\xi, \quad \alpha = z_\eta^2 + r_\eta^2, \quad \beta = z_\xi z_\eta - r_\eta r_\xi, \quad \gamma = z_\xi^2 + r_\xi^2.$$

The finite-difference equations are obtained by discretizing the above equations. All space derivatives are replaced by central differences of second-order accuracy, while the convection terms are approximated by a third-order upwind scheme (Kawamura, Takami & Kuwahara 1986), which can be described as

$$\left(f\frac{\partial u}{\partial \xi}\right)_{i,j} = f_{i,j}\frac{-u_{i+2,j} + 8(u_{i+1,j} - u_{i-1,j}) + u_{i-2,j}}{12\Delta\xi} + |f_{i,j}|\,\frac{u_{i+2,j} - 4u_{i+1,j} + 6u_{i,j} - 4u_{i-1,j} + u_{i-2,j}}{4\Delta\xi}, \tag{31}$$

where f is an arbitrary function and (i, j) denotes the grid point in the transformed plane (ξ, η). This scheme contains a numerical viscosity which can be estimated to the leading order as

$$(\Delta\xi)^3\,|f|\,\frac{\partial^4 u}{\partial \xi^4}.$$

The time increment Δt is set to be 1×10^{-3} or 2.5×10^{-3}.

3.2. *Grid generation*

In order to generate a grid, the discrete variational (DV) formulation is used. In the general DV formulation, measures of three properties of the grid are controlled: the spacing between the grid lines (F_s), the area of the grid cells (F_a), and the orthogonality of the grid lines (F_o). The grid is generated directly by solving a minimization problem resulting from a weighted combination of the three functionals (F_s, F_a, F_o):

$$\text{minimize } F = AF_s + BF_a + CF_o \quad (A, B, C \geqslant 0),$$

where A, B and C are the functional scaling factors. The resulting minimization problem is solved using a conjugate gradient iterative method developed by Castillo (1991). We set the three parameters to $A = 0.01$, $B = 0.25$ and $C = 0$.

To calculate the boundary layer structure accurately we must estimate the thickness of the velocity and the density boundary layers. As the equation for the density (11) or (23) shows, the density boundary layer is controlled by the Péclet number Pe. The density boundary layer thickness δ_d can be estimated as $O(1/\sqrt{Pe}) = O(1/\sqrt{Re\,Sc})$ (Schlichting 1968; Yih 1969), which is thinner than the viscous boundary layer for fluids with a high Schmidt number ($Sc > 1$). For salt as the stratifying medium, $Sc = 700$. Then, for $Re = 200$, the density boundary layer thickness becomes approximately $\delta_d = 0.0053$. Therefore, we concentrate the grid points near the sphere surface such that the smallest mesh size is 0.00082. Under this condition, the distance of point $(i, j) = (33, 6)$ from the sphere surface is 0.006. Therefore, there are about six points in the density boundary layer. For the same Reynolds number the viscous boundary layer thickness δ_v is estimated to be $O(1/\sqrt{Re/2}) = 0.1$, which is easily resolved by the same grid. In our grid, at 24 points away from the sphere surface, i.e. at $(i, j) = (33, 24)$, the distance from the sphere surface is $0.073(< 0.1)$. The density and velocity distributions in each boundary layer were almost unchanged when we halved the grid size near the sphere surface (see also § 4.4).

The external boundary of the grid is elliptic with a size of 40 sphere diameters in the vertical direction and 20 diameters in the horizontal direction. The grid consists of 65×90 ($\xi \times \eta$) mesh points in the (z, r)-plane. Figure 4 shows the grid near the sphere.

In order to study how the collapsing/vanishing of the rear vortex depend on the stratification, we used Froude numbers and Reynolds numbers as shown in figure 2. More specifically we used 20 Froude numbers and 40 Reynolds numbers in the range of $0.2 \leqslant F \leqslant 200$ and $10 \leqslant Re \leqslant 800$.

Nearly steady solutions defined by the convergence criterion (§ 3) were obtained at time $t = 40$–60, the indefiniteness being dependent on the Reynolds number and the Froude number. The velocity distribution in homogeneous fluids is controlled by Re and the dissipation time scale is given by $Re \times l^2$, where l is the length scale of the flow. Usually, in numerical simulations of the steady flow of homogeneous fluids, the velocity reaches steady state faster for smaller Re when some initial guess of the velocity distribution, e.g. uniform flow, is used. In our problem, the governing equations (10) and (11) have a diffusion term controlled by Pe and the density diffusion time scale is $Pe \times l^2$. In our simulation, the Schmidt number is fixed at $Sc = 700$ ($>> 1$) so that the Péclet number $Pe = Re\,Sc$ is determined only by the Reynolds number Re. Then, for a larger Reynolds number, both the dissipation time scale and the diffusion time scale become larger and it generally takes a longer time to reach the steady state. For more detailed explanation of the numerical method, the reader can refer to Torres (1997).

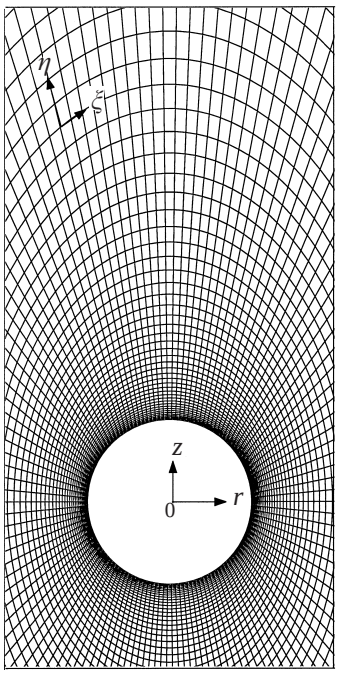

FIGURE 4. Close-up view of the grid used for the computation.

4. Results

4.1. *Vortex collapse and rear jet formation*

In figure 5 we show the typical change of flow patterns with stratification. At these moderate Reynolds numbers ($Re = 70$–200) we clearly observe the collapse of the rear axisymmetric vortex with increasing stratification.

When the stratification is very weak ($F = 200$), the flow pattern is almost identical to that of homogeneous fluid: the size of the rear vortex (see also figure 8) and the drag coefficient $C_d = 0.8$ ($Re = 200$) and $C_d = 1.36$ ($Re = 70$) (figure 11) agree well with the previous experiments for homogeneous fluids (Taneda 1956; Schlichting 1968), numerical simulations for homogeneous fluids (Chang, Liou & Chern 1992; Chang & Maxey 1994) and numerical simulations for horizontal stratified flows at $F = 200$ (Hanazaki 1988).

As the stratification becomes stronger, the rear vortex collapses. The collapse is significant even with relatively weak stratification (figure 5*b*, $F = 20$), well before the generation of strong internal waves. This shows that the phenomenon is essentially independent of internal wave generation. This is different from the horizontal stratified flow (Hanazaki 1988), in which the vortex collapse does not become significant until the stratification becomes much stronger ($F \leqslant 2$) so that large-amplitude internal waves are generated. In the present case the vortex completely collapses at $F \simeq 19$, leaving a strong downstream jet on the symmetry axis of the flow.

The mechanism of the rear jet generation can be explained as follows. Let us assume that the stratification is made up of many thin layers with slightly different densities. The layers would be deformed when the sphere passes through. All the isopycnals or the layers which existed initially in front of the sphere must accumulate very near the front surface of the sphere when the density diffusion is negligible and

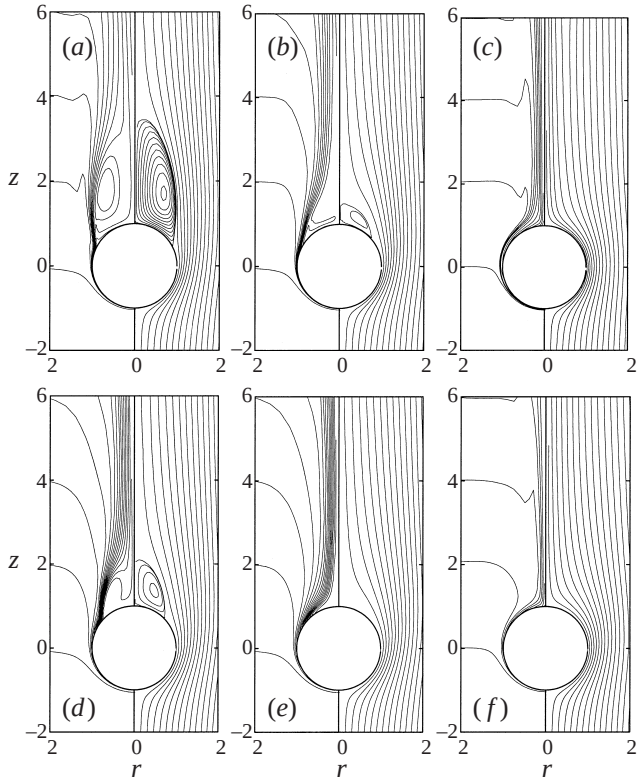

FIGURE 5. The isopycnals (left half of each figure) and Stokes streamlines (right half) for various Froude and Reynolds numbers. (*a*) $(F, Re) = (200, 200)$; (*b*) (20, 200); (*c*) (2, 200); (*d*) (200, 70); (*e*) (20, 70); (*f*) (2, 70). Isopycnals are drawn for $\rho - z = 0, -2, -4, -6, \ldots$. The contour $\rho - z = 0$ asymptotes to the line $z = 0$ in the limit $r \to \infty$. The streamlines are drawn for $\psi = 2.5 \times 10^{-3} \times n^2 (n = 0, 1, 2, \ldots)$ and for $\psi = -1.0 \times 10^{-4} \times n^2 (n = 1, 2, \ldots)$.

the density is conserved along the fluid flow direction (cf. § 2). Then the fluid in those layers pushed downward by the sphere will go back to its original position because of mass conservation, and the layers near the sphere surface have to become thinner and thinner with time.

When the layers become thin enough, the density gradient becomes large and the diffusion effects become larger and finally balance the above non-diffusive effect. Then a steady state could be reached. Figure 6 shows that a number of density contours do disappear on the sphere surface due to diffusion in the density boundary layer.

The flow around an obstacle moving vertically in a weakly stratified inviscid fluid but without buoyancy effects has been studied by Eames & Hunt (1997). They did not apply the Boussinesq approximation and investigated the solution of the momentum equation without a buoyancy term. The equation incorporated the effect of density variation only in the inertial term. They predicted, however, the appearance of attached streamlines along which the density gradient and the vorticity becomes singular. The velocity field downstream of the body showed a localized 'jet' along the centreline. The velocity of the jet was found to be proportional to the density gradients.

Our results show that these attached streamlines in reality accumulate very near the rear axis of the flow and form a strong jet. The conditions in our study are different

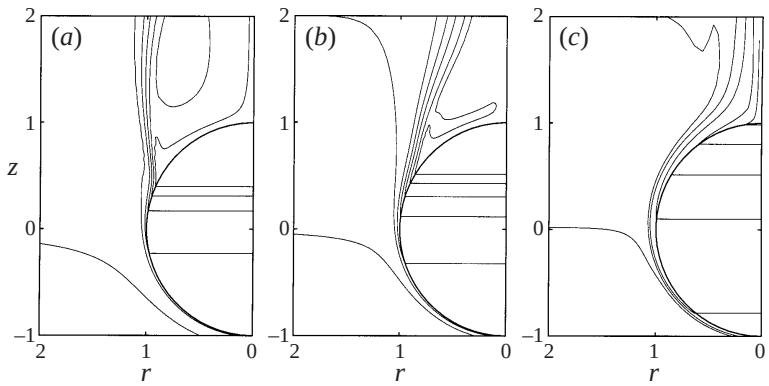

FIGURE 6. Isopycnals near the sphere ($Re = 200$). (*a*) $F = 200$; (*b*) $F = 20$; (*c*) $F = 2$. Contours are drawn for $\rho - z = 0, -2, -6, -10, -14$ and -18. The horizontal lines denote the isopycnals on the sphere surface.

from their study in that the buoyancy effect is included and the density is diffusive. While the diffusion halts the piling-up of isopycnals and prevents the generation of singularities and the jet, the strong buoyancy force generates a large vertical velocity. The flow must be unsteady in inviscid fluid, but a nearly steady state appears when density diffusion exists.

For a more direct comparison with the results of Eames & Hunt (1997) we have to include the effect of density variation in the inertial term of the momentum equation and not in the buoyancy term, without using the Boussinesq approximation. Those simulations are of much interest but beyond the scope of this study. The inclusion of density diffusion would inhibit the extreme piling up of the density surface, and prevents the generation of the jet which would appear if the fluid is non-diffusive. Thus, it is expected that the buoyancy force would be necessary to generate a jet if the fluid is diffusive.

Srdić-Mitrović *et al.* (1999) have shown that a particle descending from an upper homogeneous fluid into a stably stratified fluid drags the upper-layer light fluid into the stratified layer and generates a caudal fluid column. After sufficient intrusion into the stratified layer, however, the film which surrounds the particle and the caudal fluid column is ruptured. Then, the detached film rises and most of the dragged fluid goes back to the upper homogeneous layer. In the present study, similar processes, including the rupture of the light-fluid column and the subsequent detachment from the sphere appear. But those processes occur continually along with the continual dragging of the upper light fluid, and a nearly steady state can be reached.

The fluid in the continually ruptured layers goes up in a thin layer that surrounds the boundary layer and it finally forms a jet on the rear axis of the sphere. This is shown in figure 7, where the downstream velocities are shown for low Froude numbers ($F \leqslant 2$). Comparison of figure 7(*a*) ($F = 2$) with figure 7(*b*) ($F = 1$) or 7(*c*) ($F = 0.2$) shows that the width/radius of the jet decreases with decreasing Froude number in qualitative agreement with the experiments (cf. figure 1). The maximum speed in the jet is $w = 8.3$–9.4 in the parameter range of $0.4 \leqslant F \leqslant 2$, showing a rather weak dependence on F.

For much lower Froude numbers ($F \leqslant 0.4$), the speed of the jet increases considerably. At $F = 0.2$ (figure 7*c*) the maximum speed is $w = 14$ and it increases up to $w = 20$ for the lowest Froude number ($F = 0.1$) investigated in this study. Since

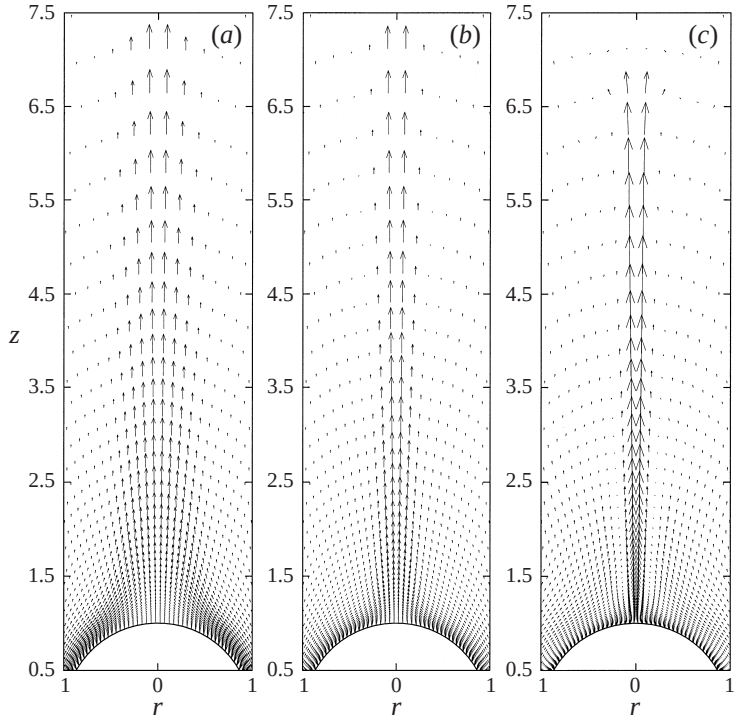

FIGURE 7. Velocity distributions in the rear jet observed at low Froude numbers ($Re = 200$). (a) $F = 2$; (b) $F = 1$; (c) $F = 0.2$.

the potential energy attained by the fluid is large when the stratification is strong, the kinetic energy converted from the potential energy is large in strongly stratified fluid. Then the velocity of the vertical jet is expected to become generally larger with increasing stratification.

The Reynolds numbers used in the numerical simulations are lower than in the experiments by Ochoa & Van Woert (1977, cf. figure 1) but the mechanism of vortex collapse and jet formation would be the same. In the experiments for $Re \approx 800$, complete collapse of the vortex occurs at $F \approx 10$ (figure 1b). The threshold value of F for complete collapse becomes somewhat lower for larger Reynolds numbers, since the original size and strength of the rear vortex is larger for larger Reynolds numbers and stronger stratification becomes necessary to collapse the vortex. In our numerical simulations, the results for $Re = 70$ show complete collapse of the rear vortex at $F = 20$, while for $Re = 200$ there is no complete collapse at the same Froude number.

It is of interest, however, to note that the critical Froude number F_c for complete collapse is rather independent of the Reynolds number and the value is generally around $F_c = 20$ (cf. figure 16). This illustrates that the collapse is essentially an effect of stratification and the viscous effects are of secondary importance. This can be seen also in figure 8, where the separation angle of the boundary layer is shown for a wide range of Froude numbers ($0.01 < 1/F < 10$) and three representative Reynolds numbers. This figure shows that in homogeneous fluids ($1/F \ll 1$) the separation angles θ_s agree with the previous studies. For example, $\theta_s = 65^\circ$ for $Re = 200$ and $\theta_s = 42^\circ$ for $Re = 50$ in agreement with the experiments by Taneda (1956). The

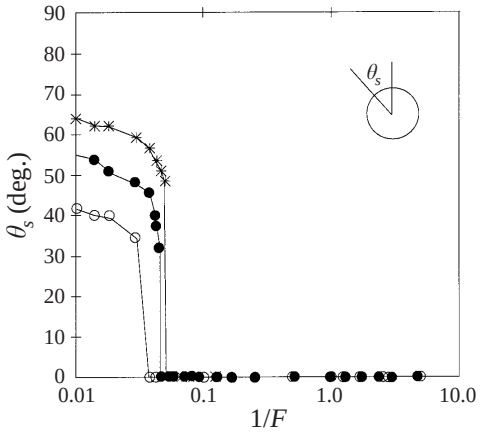

FIGURE 8. Separation angle θ_s as a function of $1/F$ for three representative Reynolds numbers. ○, $Re = 50$; ●, $Re = 100$; and *, $Re = 200$.

figure also shows that complete collapse of the standing vortex occurs at only slightly stronger stratifications for higher Reynolds numbers.

Our simulations (Torres *et al.* 1999) performed for larger Reynolds numbers ($Re >$ 200) with weak stratification ($F = 200$) showed good agreement with the numerical study of Fornberg (1988) for homogeneous fluids. The experiments for homogeneous fluids show that the rear standing vortex becomes unstable for $Re \gtrsim 500$ and the downstream flow becomes non-axisymmetric. In the presence of stratification, however, the rear vortex is first collapsed by stratification and a rear jet is generated. Then, approximately axisymmetric flows have been observed even at rather high Reynolds numbers ($Re \geqslant 800$) as already shown in figure 1.

Finally it is important to note that, even after the complete collapse of the rear vortex ($F < 20$), large vorticity actually exists within the rear jet, although the flow pattern resembles a potential flow with fore-and-aft symmetry. Therefore, the flow is not at all irrotational at low Froude numbers. This is again consistent with the results of Eames & Hunt (1997), in which the singularity of vorticity along the rear axis is predicted, although such a singularity may not exist when there is density diffusion.

4.2. *Lee waves*

In figure 9, our numerical results at low Froude numbers ($Re = 200$) are compared with the experiments by Mowbray & Rarity (1967), the only experiment that we know of in which the lee wave patterns generated by a vertically moving obstacle have been investigated. Our lee wave patterns, which are almost steady at low Reynolds numbers, agree well with their shadowgraphs in spite of the possible difference in the Reynolds number. In Mowbray & Rarity (1967), the Reynolds numbers were kept less than 200 but more specific values are not given in their paper.

Applying the principle of stationary phase to the linear wave solutions presented in an integral form, we can define from which points the major contribution to the integral come (Mowbray & Rarity 1967; see also Lighthill 1978). Those points constitute a line of constant phase and the equations for its coordinates (r, z) are

$$r = F\Phi \left(\frac{\sigma^{-4} + \sigma^{-2} - 1}{1 + \sigma^2(2 - \sigma^2)^2(1 - \sigma^2)^{-3}} \right)^{1/2}, \tag{32}$$

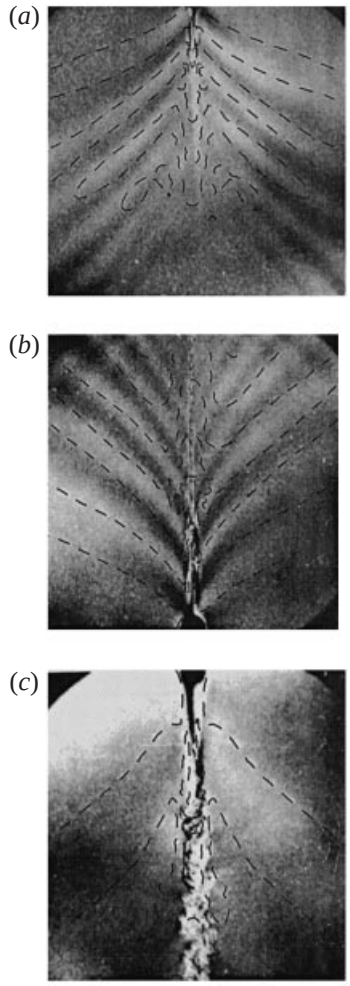

FIGURE 9. Comparison of the isopycnals obtained in this numerical study with shadowgraphs by Mowbray & Rarity (1967). The isopycnals given by dashed lines in each figure show the contours of zero density perturbation $\rho = 0$ obtained by numerical simulation at $Re = 200$ and the shadowgraphs were taken at $Re \leqslant 200$ but exact values of Re are uncertain. (*a*) $F = 0.4$; (*b*) $F = 0.59$; (*c*) $F = 2$.

and

$$z = F\Phi\sigma(2-\sigma^2)(1-\sigma^2)^{-3/2}\left(\frac{\sigma^{-4}+\sigma^{-2}-1}{1+\sigma^2(2-\sigma^2)^2(1-\sigma^2)^{-3}}\right)^{1/2}, \tag{33}$$

where Φ is the phase and σ $(0 < \sigma < 1)$ is a variable parameter. The wave amplitude will be zero at $\Phi = n + \pi/4$ $(n = 0, 1, 2, \ldots)$.

Figure 10 shows the comparison of lines of constant phase ($\Phi = n + \pi/4$, $n = 0, 1, 2, \ldots$) obtained from the linear theory and the corresponding contours of zero-density-perturbation lines ($\rho = 0$) obtained by numerical simulations. The agreement is generally good. The results for the lines $\Phi = \pi/4$ show rather poor agreement for $F \leqslant 2$ but this can be explained by the fact that the method of stationary phase is applicable only to the far field. It is of interest to note that the lee wave wake, the diverging pattern of the density contours, appears even at weak stratifications (e.g.

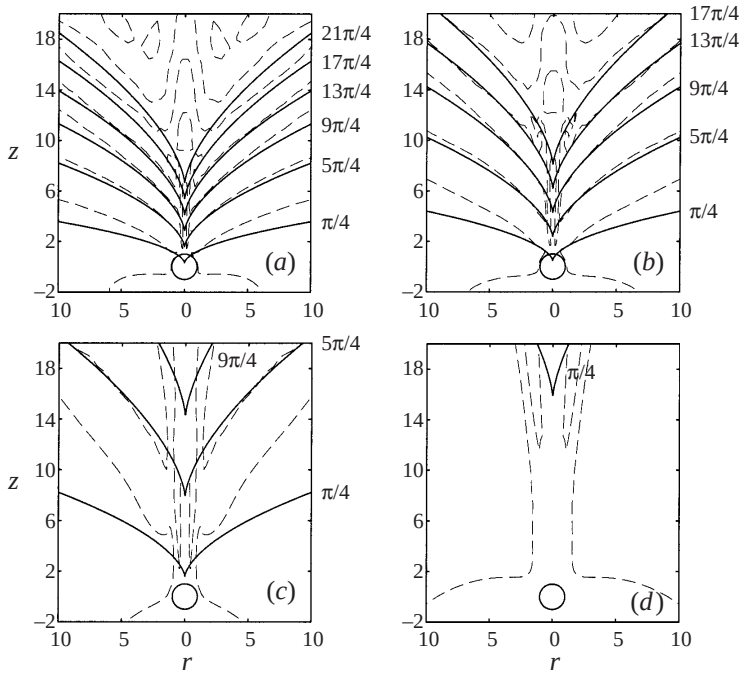

FIGURE 10. Comparison of the isopycnals of $\rho = 0$ obtained by this numerical study (dashed lines) at $Re = 200$ with the lines of constant phase obtained by the linear wave theory (solid lines). The contours are drawn for phase $\Phi = (n + 1/4)\pi$, $(n = 0, 1, 2, \ldots)$. (*a*) $F = 0.4$; (*b*) $F = 0.6$; (*c*) $F = 2$; (*d*) $F = 20$.

$F = 20$). Numerical results actually show a similar diverging lee wave wake at very weak stratification ($F = 200$), although the results are not presented here. It should also be noted that the method of stationary phase predicts that the wave amplitude decreases in proportion to $d^{-1/2}$, where d is the distance from the obstacle. Then the wave amplitude in the far field decreases, without viscosity and diffusion.

4.3. *Drag coefficient of the sphere*

The drag acting on a body can be calculated as a surface integral of normal and shear stresses and it can be separated into two parts. One is the pressure drag coefficient C_p due to the pressure distributions and the other is the frictional drag coefficient C_f, which represents the contribution from the tangential stresses.

To be explicit, these two coefficients are calculated from the formulae

$$C_p = \frac{1}{\frac{1}{2}\rho_o W^2 \pi a^2} \int_S (-p\delta_{i,k}) n_k \, \mathrm{d}S, \tag{34}$$

and

$$C_f = \frac{1}{\frac{1}{2}\rho_o W^2 \pi a^2} \int_S \mu \left(\frac{\partial u_i}{\partial x_k} + \frac{\partial u_k}{\partial x_i} \right) n_k \, \mathrm{d}S, \tag{35}$$

where i denotes the mean flow direction (vertically upward), n_k is the component of the unit vector normal to the sphere surface and $\mathrm{d}S$ is the area unit of the surface integral. The total drag coefficient C_d is given by the sum of C_p and C_f.

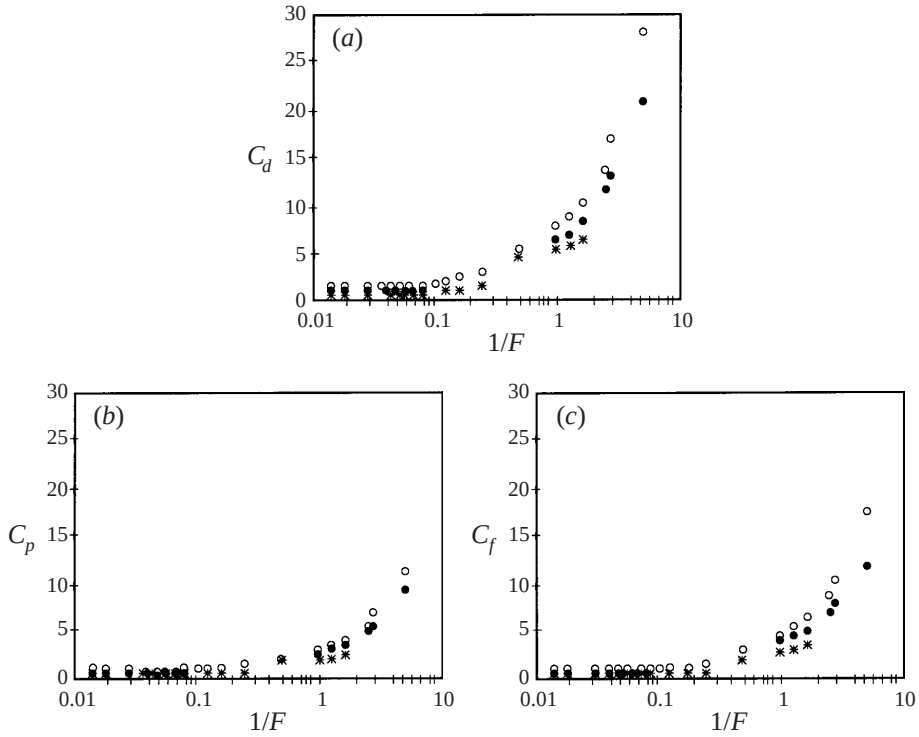

FIGURE 11. Froude number dependence of the drag coefficients: (*a*) total drag coefficient, C_d; (*b*) pressure drag coefficient, C_p; (*c*) frictional drag coefficient, C_f. Each plot is for three representative Reynolds numbers. ○, $Re = 50$; •, $Re = 100$; *, $Re = 200$.

Figure 11 shows the Froude number dependence of C_d, C_p and C_f for three representative Reynolds numbers. These three coefficients all increase monotonically with increasing stratification, i.e. with increasing $1/F$.

It is of interest to note that the increase of the drag coefficient C_d is rather small until the complete collapse of the rear vortex occurs at $F \sim 20$ (cf. figure 8); then it increases considerably ($F < 20$). Although the drag increases due to the rearward movement of the separation point and the subsequent change in the pressure and shear stress distributions, their effect leads to only less than about a 25% increase compared to the unstratified drag. For example, at $Re = 200$, the value of C_d at $F = 10$ is about 1.0, only 25% larger than the unstratified value $C_d = 0.8$. The drag increases rapidly for $F < 10$ ($1/F > 0.1$) and it reaches more than ten times its homogeneous counterpart at $F = 0.2$.

To investigate the mechanism of the considerable increase of drag for $F < 10$ ($1/F > 0.1$), we plot the contours of dynamic pressure in figure 12. Comparison of figure 12(*a*) ($F = 200$) with figure 12*b–d* ($F = 2, 1, 0.4$) shows that the pressure contours at low Froude numbers accumulate near the rear stagnation point of the sphere, showing the significant pressure reduction there (see also figure 13). This causes the drag increase at low Froude numbers. At the lowest Froude number described ($F = 0.4$), the pressure distributions also show the lee wave patterns identified in the density contours (cf. figure 10*a*). It is of interest to note that at $F = 2$ (figure 12*b*) the pressure near the equator ($z \approx 0$) is higher than at $F = 200$. This anomalous pressure distribution can be explained by Bernoulli's theorem developed below.

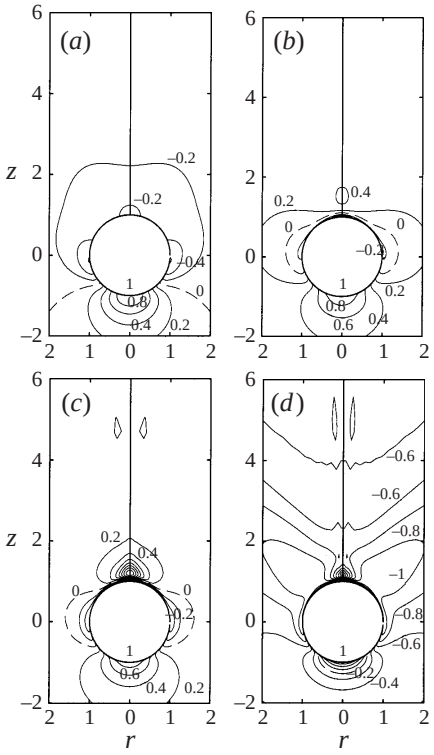

FIGURE 12. The dynamic pressure distributions near the sphere at $Re = 200$. (*a*) $F = 200$; (*b*) $F = 2$; (*c*) $F = 1$; (*d*) $F = 0.4$. Interval of the contours is $\Delta p = 0.2$. The dynamic pressure at the fore stagnation point is fixed to be $p = 1$. The dashed line is the line of $p = 0$.

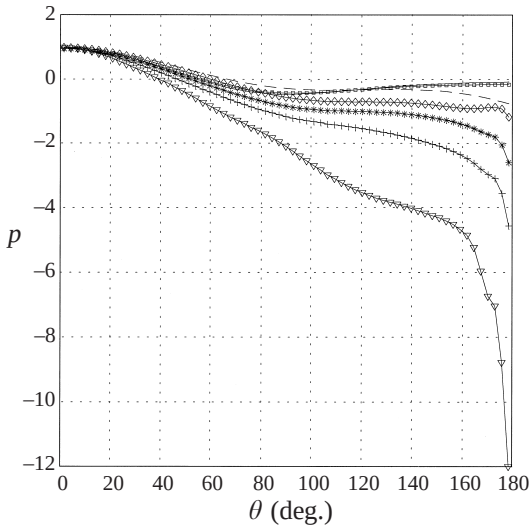

FIGURE 13. Pressure distribution on the sphere surface for various Froude numbers ($Re = 200$). In this figure the angle θ is measured from the fore stagnation point. ——, $F = 200$; □, $F = 20$; ––, $F = 2$; ◇, $F = 1$; *, $F = 0.6$; +, $F = 0.4$; ▽, $F = 0.2$.

Let us consider a streamline originating upstream near the centre axis of the flow. Bernoulli's theorem for steady inviscid Boussinesq fluid can be derived from (10) and (11) in the limit of $Re \to \infty$ and $Pe \to \infty$ as

$$\frac{\partial}{\partial s}\left(p + \tfrac{1}{2}\boldsymbol{u}^2\right) = -\frac{\rho}{F^2}\frac{\partial z}{\partial s}, \tag{36}$$

where s is the coordinate along the steady streamline.

According to this theorem, the sum of pressure and kinetic energy per unit volume changes due to the source term on the right-hand side of equation (36), which represents the effect of stratification. Since the source term can be rewritten as

$$\frac{\partial z}{\partial s} = \frac{w}{|\boldsymbol{u}|}, \tag{37}$$

it takes a positive large value near the equator of the sphere ($z = 0$) where $w/|\boldsymbol{u}| \simeq 1$ and the perturbation density ρ is negative. Then the total head increases along the streamlines near the equator. This means the possibility of the simultaneous increase of the velocity $\boldsymbol{u}$ and the dynamic pressure, which could explain why in the case of $F = 2$, the pressure can be larger than the case of $F = 200$ even when the large velocity leading to the rear jet (cf. figures 7*a*, 14) is induced.

As the fluid approaches the rear stagnation point, the source term becomes small ($\partial z/\partial s \simeq 0$) but it becomes large again on the rear axis of the flow where $w/|\boldsymbol{u}| \simeq 1$ and $\partial z/\partial s \simeq 1$. Since the density perturbation ρ is negative and its modulus $|\rho|$ becomes larger near the axis, the acceleration effect is largest when the fluid particle moves along the rear axis. Then the vertical fluid movement is most accelerated along the rear axis, generating a vertical jet.

Near the rear stagnation point, the pressure becomes very low. Since the source term is small near the stagnation point, the reduction of the pressure directly corresponds to the increase of velocity, which leads to the generation of a strong vertical jet. To see this process, the pressure distribution on the sphere is shown in figure 13 for various Froude numbers ($Re = 200$). For weak stratification ($F = 200$), the separation point of the boundary layer is almost identical to the unstratified case and it is located somewhat downstream of the point where the pressure gradient reverses sign. At lower Froude numbers ($F \leqslant 1$) there is a clear decrease of the pressure near the rear stagnation point. The pressure reduction becomes more significant for lower Froude numbers, corresponding to the formation of a stronger jet.

The inviscid lee wave drag has been studied theoretically by Warren (1960). He applied a linear approximation and used integral transform methods to solve the equation of motion, then used the methods of steepest descents and stationary phase to obtain the internal wave field in the limit of $t \to \infty$. He found that C_d ($= C_p$) increases with decreasing F, except for the extremely small Froude numbers ($F \ll 0.1$) where the drag decreases again and tends to zero (cf. his figure 16). The increase of drag is in agreement with our results. However, there is a large quantitative difference. His results show $C_d \simeq 0.1$ at $F = 1$ and $C_d \simeq 6.8$ at $F = 0.2$, but our results show much larger increase in C_d. A formal reason would be the nonlinear effects neglected in the theory, but more direct explanation is the failure of the theory in predicting the jet formation observed in our study.

In an experiment on the unsteady descent of a particle, Srdić-Mitrović *et al.* (1999) estimated the drag coefficient in 'steady' flow using a formula commonly used in multi-phase flow analysis. The formula accounts for the unsteadiness of the mean flow and represents a balance between the inertial force and the sum of the buoyancy force,

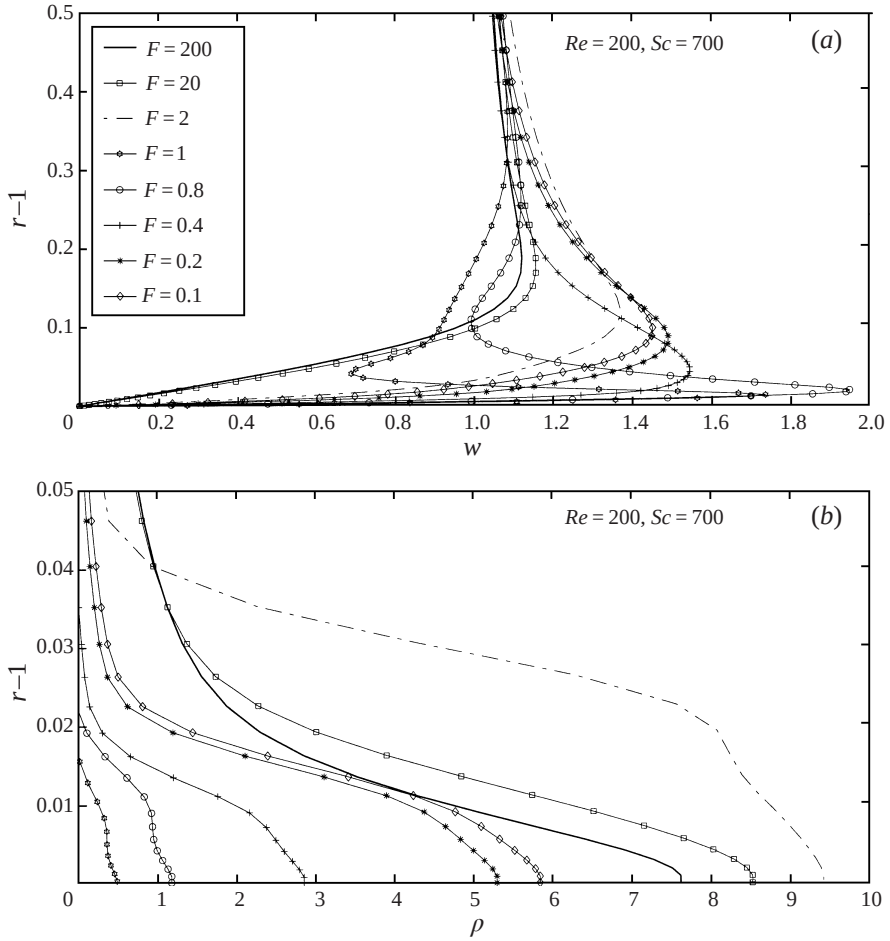

FIGURE 14. Distribution of (*a*) the vertical velocity w and (*b*) density perturbation ρ near the sphere for various Froude numbers, on the line $z = 0$. The symbols within the box apply to both figures.

steady drag, added-mass effect and the history (Basset) term. The results obtained by using that formula were compared with the total static buoyancy force exerted on the caudal fluid column. The difference was small and they concluded that the observed drag increase, which is an order of magnitude larger than its homogeneous counterpart, is mainly due to the static effect of the buoyancy force on the caudal fluid and that the internal-wave contribution to the drag was small.

The result is consistent with our results where the drag coefficient was calculated directly. This shows that the rear caudal fluid column or the filament/jet is essential to the significant increase of drag coefficient. In the experiments of Srdić-Mitrović *et al.* (1999), the significant drag increase was observed at rather weak stratifications ($3 < F < 10$). In our study some drag increase was observed for $F < 10$, but very rapid increase was not observed until much lower Froude numbers ($F < 1$). This would be due to the difference in the mean vertical density distribution investigated. The caudal fluid column in the experiments of Srdić-Mitrović *et al.* (1999) is the result of the dragging of upper homogeneous fluid into the stratified interfacial layer,

so that the primary factor is the sudden change of density gradient and may not be the continuous density gradient of the stratified layer. On the other hand, the rear jet observed in our study is the result of the continual dragging and rupture of the thin layers of lighter fluids. Then the stratification strength itself is of importance in determining the flow configurations. It is of interest, however, that the large stratification drag can be explained similarly by the generation of the caudal fluid column or the round jet, independent of the precise mechanisms by which they have been generated.

In the experiments of Srdić-Mitrović *et al.* (1999), the caudal fluid column and the subsequent drag increase were observed only in the range of $1.5 < Re < 15$ ($3 < F < 10$). At high $Re\,(> 15)$, the particle drags only an insignificant amount of upper-layer fluid because of the flow separation behind the particle, so that the drag showed a satisfactory agreement with that in homogeneous fluids. In our study of continuously stratified fluids, the dragging of the upper layer occurred even at high Reynolds numbers ($Re > 15$). As is shown in figure 6(a, b), dragged fluid exists in a continuously stratified fluid even when flow separation exists. The dragging of the upper-layer fluid was probably not observed in the above experiments because the dragged layer is thin when flow separation exists. Since the volume of dragged fluid was small, its effect on the drag would have been small. In continuously stratified fluids, most fluid is dragged at low Froude numbers even after the flow separation has been completely suppressed. Then significant drag increase was observed at sufficiently low Froude numbers ($F < 1$).

At low Reynolds numbers ($Re < 1.5$), dragging of fluid was not observed in the experiments of Srdić-Mitrović *et al.* (1999) because the slow descent of particles allowed them to adjust to background conditions. This implies that the effect of density diffusion prevented the formation of the caudal fluid. In our study the Reynolds number was not less than 10 and the low Reynolds number effect was not investigated. However, in completely continuously stratified fluids, the continual breakup of the dragged density layers due to diffusion is followed by the continual generation of the newly dragged layers, so that we can expect similar dragging of the upper fluid even at low Reynolds numbers.

Comparison of figure 11(b) with figure 11(c) further shows that a larger contribution to the total drag coefficient C_d comes from C_f than C_p. This is an indication that the drag increase is due to the high-velocity flow along the sphere surface which contributes to C_f (cf. figure 14), in addition to the direct pressure reduction on the rear surface which contributes to C_p.

4.4. *Velocity and density boundary layers*

Figure 14 shows how the distributions of vertical velocity and density perturbation ($Re = 200$) near the sphere surface vary with the Froude number. As was mentioned in § 3.2, the theoretical estimation of the velocity boundary layer thickness is $\delta_v = 0.1$ and the density boundary layer thickness is $\delta_d = 0.0053$. The thickness of the velocity boundary layer ($\delta_v \sim 0.1$) agrees well with the theoretical prediction, while the density boundary layer thickness ($\delta_d = 0.02$) is several times thicker. This makes unnecessary the use of an extremely fine grid and makes the computation somewhat easier. Indeed we have tested a computational grid with half mesh size, but the density distributions in the density boundary layer generally showed quantitatively negligible differences.

When leaving the sphere surface (figure 14a), w increases from zero to a maximum value which generally becomes larger for lower Froude numbers. At the same time,

the velocity boundary layer becomes thinner with stratification. For very low Froude numbers ($F = 0.1, 0.2$), w oscillates in the r-direction. The region of $w < 1$ exists to compensate for the very large velocity near the surface and the oscillation is closely related to the appearance of internal waves near the line $z = 0$ at very strong stratification ($F \leqslant 0.2$). This trend could also be identified in figure 10, which shows that the line $\Phi = \pi/4$ moves nearer to $z = 0$ with increasing stratification. Far from the surface ($r - 1 > 0.3$), w asymptotes to its mean flow value ($w = 1$). These phenomena are consistent with jet formation along the sphere surface as described in § 4.1 which corresponds to the low pressure at low Froude numbers ($F \leqslant 2$) as described in § 4.3.

On the other hand, the thickness of the density boundary layer is rather independent of the stratification. At weak stratification ($2 \leqslant F \leqslant 200$) the thickness increases with the collapse of the rear vortex. As is shown in figure 6, the distance between isopycnals becomes larger with the rearward movement of the separation point. The isopycnals which accumulate near the separation point at weak stratifications become sparse due to the collapse of the rear vortex and the subsequent movement of the isopycnals nearer to the rear stagnation point. This results in the thicker density boundary layers.

With the further decrease of F, however, the thickness decreases again to the unstratified level, and for very strong stratification ($F \leqslant 1$), there is a significant decrease of the perturbation density ρ at the sphere surface ($r - 1 = 0$) and it asymptotes to zero in the low Froude number limit. This corresponds to almost horizontal isopycnals even very near the obstacle.

5. Conclusions

The flow around a sphere moving vertically in stratified fluid has been studied numerically. We found the complete collapse of the standing vortex behind a sphere when the stratification is strong. Our numerical simulations clarified that a thin filament behind a sphere found in the visualization experiments by Ochoa & Van Woert (1977) is actually a strong vertical jet on the rear axis of the flow.

The processes of vortex collapse and jet formation have some similarities to non-diffusive mechanisms. If density is conserved along the flow, all the isopycnals that existed initially in front of the downward moving sphere accumulate very near its front surface indefinitely with time, and they generate a singularity along the rear axis of the flow, generating a vertical jet. This process has been predicted by Eames & Hunt (1997) for inviscid flow without a buoyancy effect.

However, when there is density diffusion as described in this study, the piling-up of the isopycnals is halted at some level so that steady state is realized, and the singularities on the rear axis do not appear. Therefore, the jet will not be generated without a buoyancy force. The strong jets observed in this study most likely have their origin in the conversion of potential energy to vertical kinetic energy.

The observed rear jet contributes to the significant increase of the drag coefficient, reaching more than ten times its homogeneous counterpart at very low Froude numbers ($F \leqslant 0.2$). A similar increase of the drag has been observed by Srdić-Mitrović *et al.* (1999) when a sphere descends from a homogeneous layer into a stratified fluid. They observed significant drag increase at much weaker stratifications ($3 < F < 15$) since the dragging of the upper layer fluid occurred even at weak stratifications. The drag increase was transient, however, since the caudal fluid column is ruptured and successive dragging of the upper fluid does not occur in their context.

In this study for completely continuously stratified fluid, the dragging of the upper-

layer fluid and the rupture of the dragged layers due to diffusion occurs successively and the high-drag states continue steadily. However, it is of interest to note that the large drag increase can be explained similarly by the generation of the caudal fluid column or the jet, independent of their generation mechanisms.

This study is an extension of the PhD thesis of C.T., which has been supported by Universidad Autónoma de Baja California under grant 4031 and Consejo Nacional de Ciencia y Tecnología under grants E1421-D920 and through program of Inicio a la Investigación I27039-T respectively. Partial support for the computational facilities has been provided by CONACYT under grant 28794-T. We would like to acknowledge the discussions with Federico Graef and Julio Sheinbaum. We are also grateful for the use of the equipment and facilities of the Hydraulic Laboratory of Scripps Institution of Oceanography and thank Clint Winant who suggested the experiment by Ochoa & Van Woert (1977) and for his comments.

Appendix

Two of the present authors did a series of experiments in a $1\,\mathrm{m}^3$ cubic tank, slowly lowering and raising at different speeds acrylic spheres of different sizes suspended by a thin wire in linearly stratified salt water (Ochoa & Van Woert 1977). The stratification was made by quickly stirring an initially two-layer system, fresh on top, salty below, then waiting until it settled completely. The density stratification was measured by a conductivity probe, taking samples at about every 10 cm vertically in the tank, and calibrated against bucket samples with an hydrometer. The speed was set by a calibrated variable motor.

Figure 15 shows typical shadowgraphs of sphere wakes taken at rather high Reynolds numbers. At $Re = 1524$ and $F = 12.62$ (figure 15*a*) we can observe filaments downstream of the sphere. This, along with figure 1, shows the approximate axisymmetry of the flow at rather high Reynolds numbers ($Re \geqslant 762$). In some shadowgraphs (figure 15*b*), the collapse of the rear vortex was incomplete at higher Reynolds numbers ($Re = 1900, F = 15.79$), but the vortex was almost completely collapsed at a lower Froude number (figure 15*c*) with approximately the same Reynolds number. Figure 15*c* shows, however, a meandering of the filament, showing that this is an asymmetric wake (cf. see figure 16). Figure 15*d* shows a turbulent wake at a higher Reynolds number $Re = 2667$ ($F = 14.9$) with a Froude number similar to figure 15(*b*). These figures indicate that in the presence of density stratification the transition to turbulence occurs at higher Reynolds numbers than in homogeneous fluids.

Figure 16 shows the parameters investigated in the experiments by Ochoa & Van Woert (1977). The dashed line, which separates the two parameter regions with and without rear filaments/jets, shows that the critical Froude number necessary for the complete collapse of the rear vortex decreases with increasing Reynolds number. This increase is more rapid than the numerical results with the axisymmetry assumption and at lower Reynolds numbers ($Re \leqslant 1000$). The difference may be due to the assumption of axisymmetry applied in the numerical simulation, which will reduce the critical Froude number in the Reynolds number range of $200 \leqslant Re \leqslant 1000$. If the flow is not axisymmetric, stronger stratification would be necessary to suppress the rear vortical wake.

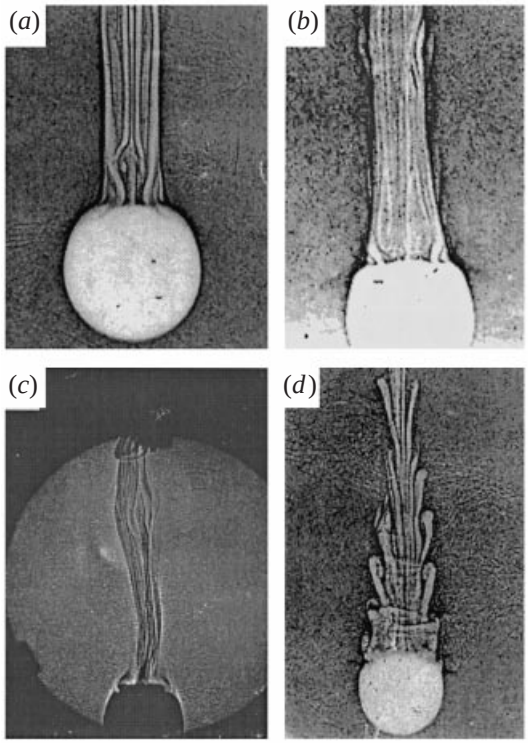

FIGURE 15. Shadowgraphs of the sphere wakes at high Reynolds numbers. (*a*) $(F, Re) = (12.64, 1524)$; (*b*) (15.79, 1900); (*c*) (10.54, 1905); (*d*) (14.9, 2667).

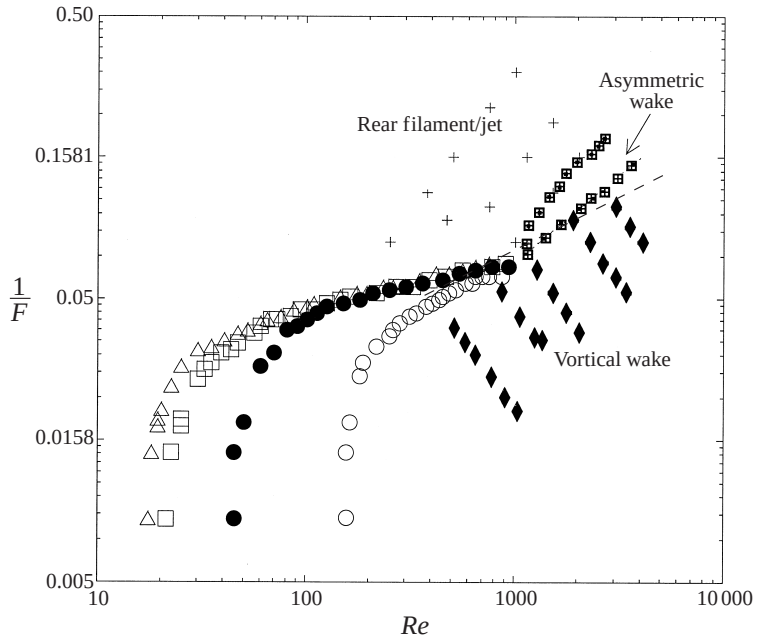

FIGURE 16. An enlargement of the diamond region depicted in figure 2 which shows the experimental results by Ochoa & Van Woert (1977): ◆, vortical wake; +, rear filament/jet. The region where a non-axisymmetric wake was observed is shown by an arrow. Separation angle, θ_s, measured from the rear stagnation point obtained in this numerical study is also shown. △, $\theta_s = 10$; □, $\theta_s = 20$; •, $\theta_s = 40$; ○, $\theta_s = 60$.

REFERENCES

Achenbach, E. 1974 Vortex shedding from spheres. *J. Fluid Mech.* **62**, 209–221.

Billet, D. S., Lampitt, R. S., Rice, A. L. & Mantoura, R. 1983 Seasonal sedimentation of phytoplankton to the deep-sea benthos. *Nature*, **302**, 520–522.

Castillo, J. E. 1991 A discrete variational grid generation method. *SIAM J. Sci. Statist. Comput.* **12**, 454–468.

Chang, C.-C., Liou, B.-H & Chern, R.-L. 1992 An analytical and numerical study of axisymmetric flow around spheroids. *J. Fluid Mech.* **234**, 219–245.

Chang, E. J. & Maxey, M. R. 1994 Unsteady flow about a sphere at low to moderate Reynolds number. Part 1. Oscillatory motion. *J. Fluid Mech.* **277**, 347–379.

Chomaz, J. M., Bonneton, P. & Hopfinger, E. J. 1993 The structure of the near wake of a sphere moving horizontally in a stratified fluid. *J. Fluid Mech.* **254**, 1–21.

Eames, I. & Hunt, J. C. R. 1997 Inviscid flow around bodies in weak density gradients without buoyancy effects. *J. Fluid Mech.* **353**, 331–355.

Fornberg, B. 1988 Steady viscous flow past a sphere at high Reynolds numbers. *J. Fluid Mech.* **190**, 471–489.

Graf, G. 1989 Benthic-pelagic coupling in a deep-sea benthic community. *Nature* **341**, 437–439.

Hanazaki, H. 1988 A numerical study of three-dimensional stratified flow past a sphere. *J. Fluid Mech.* **192**, 393–419.

Hanazaki, H. 1989 Upstream-advancing columnar disturbances in two-dimensional stratified flow of finite depth. *Phys. Fluids* A **1**, 1976–1987.

Hanazaki, H. 1994 On the three-dimensional internal waves excited by topography in the flow of a stratified fluid. *J. Fluid Mech.* **263**, 293–318.

Harlow, F. H. & Welch, J. E. 1965 Numerical calculation of time-dependent viscous incompressible flow of fluid with free surface. *Phys. Fluids* **8**, 2182–2189.

Hunt, J. C. R. & Snyder, W. H. 1980 Experiments on stably and neutrally stratified fluid over a model three-dimensional hill. *J. Fluid Mech.* **96**, 671–704.

Kawamura, T., Takami, H. & Kuwahara, K. 1986 Computation of high Reynolds number flow around a circular cylinder with surface roughness. *Fluid Dyn. Res.* **1**, 145-162.

Lighthill, M. J. 1978 *Waves in Fluids*. Cambridge University Press.

Lin, Q., Lindberg, W. R., Boyer, D. L. & Fernando, H. J. S. 1992 Stratified flow past a sphere. *J. Fluid Mech.* **240**, 315–354.

Lofquist, K. E. & Purtell, L. P. 1984 Drag on a sphere moving horizontally through a stratified liquid. *J. Fluid Mech.* **148**, 271–284.

Mowbray, D. E. & Rarity, B. S. H. 1967 The internal wave pattern produced by a sphere moving vertically in a density stratified liquid. *J. Fluid Mech.* **30**, 489–495.

Ochoa, J. L. & Van Woert, M. L. 1977 Flow visualization of boundary layer separation in a stratified fluid. Unpublished report, Scripps Institution of Oceanography, pp.28.

Schlichting, H. 1968 *Boundary-Layer Theory*, 6th edn. McGraw-Hill.

Srdić-Mitrović, A. N., Mohamed, N. A. & Fernando, H. J. S. 1999 Gravitational settling of particles through density interfaces. *J. Fluid Mech.* **381**, 175–198.

Taneda, S. 1956 Experimental investigation of the wake behind a sphere at low Reynolds numbers. *J. Phys. Soc. Japan.* **11**, 1104–1108.

Torres, C. R. 1997 On the behavior of a sphere in stratified fluids. PhD Thesis (in Spanish), Centro de Investigación Científica y de Educación Superior de Ensenada, B. Cfa. México, 103 pp.

Torres, C. R., Ochoa, J., Castillo, J. & Hanazaki, H. 1999 Numerical simulation of flow past a sphere in vertical motion within a stratified fluid. *J. Comput. Appl. Maths* **103**, 67–76.

Warren, F.W.G. 1960 Wave resistance to vertical motion in a stratified fluid. *J. Fluid Mech.* **7**, 209–229.

Yih, C. S. 1969 *Fluid Mechanics. A Concise Introduction to the Theory*. McGraw-Hill.